Radio Science, Volume 13, Number 1, pages 167-187, January-February 1978

Early results from the DNA Wideband satellite experiment—Complex-signal scintillation

E. J. Fremouw[1], *R. L. Leadabrand, R. C. Livingston, M. D. Cousins, C. L. Rino, B. C. Fair, and R. A. Long*

SRI International, Menlo Park, California 94025

(Received March 16, 1977.)

A multifrequency (ten spectral lines between VHF and *S* band) coherent radio beacon is presently transmitting continuously from a 1000-km, high-inclination orbit for the purpose of characterizing the transionospheric communication channel. Its high phase-reference frequency (2891 MHz) permits direct observation of complex-signal scintillation, and its very stable, sun-synchronous orbit allows repeated pre-midnight observations at low latitudes and near-midnight observations at auroral latitudes. We present here early results of the observations; salient points include the following. First, most of the data are consistent with phase-screen modeling of the production of ionospheric scintillation, including an f^{-2} frequency dependence for phase variance. Second, propagation theories invoking weak, single scatter seldom are adequate, because even moderate intensity scintillation usually is accompanied by phase fluctuations comparable to or greater than a radian. Third, under conditions producing GHz scintillation (near the geomagnetic equator), lower frequencies show marked diffraction effects, including breakdown of the simple f^{-2} behavior of phase variance and loss of signal coherence across a band as narrow as 11.5 MHz at UHF.

1. INTRODUCTION

1.1. *Objectives.* On 22 May 1976, satellite P76-5 was launched into near-polar orbit for the sole purpose of carrying a multifrequency, coherent radio beacon (DNA-002) into a 1000-km orbit for transionospheric propagation studies. The spacecraft is a modified Navy Navigation Satellite that was stripped of its navigation-data modulators and augmented with a 1.5-m ground screen for earth-coverage radiation of 10 CW signals from the payload. The mutually coherent signals, which range from VHF to *S* band, are being recorded at ground stations in Alaska, Peru, and the mid-Pacific; initial observations were made in California.

The experimental program, called the DNA Wideband satellite experiment was conceived, designed, constructed, and fielded by Stanford Research Institute for the Defense Nuclear Agency (DNA). The program objective is to extensively characterize the perturbations (mainly scintillations) imposed on passing radio waves by structured plasmas such as those found in the ionosphere at auroral and equatorial latitudes. The nature of deleterious systems effects arising from such perturbations depends on the time structure of the resulting signal fluctuations. For example, if the scintillation rate is comparable to or greater than the time spent in transmitting one data bit, the modulation will be distorted and errors will result. The severity of performance degradation in this fast-fluctuation regime depends critically on the type of modulation used.

In many communication systems, the bit transmission rate is much greater than the scintillation rate. For such systems, phase scintillation is of little concern and amplitude fading is of primary interest. For other types of systems (such as synthetic aperture radars and certain kinds of positioning systems), phase is very important. A key element of the Wideband experiment is to provide information on scintillation of the full complex signal, in the form of both high-time-resolution records and reduced-data synopses. Besides intensity and phase scintillation indexes at the various frequencies, second-order statistical measures are being obtained in the temporal, spatial, and spectral domains.

The second-order temporal statistics are being characterized in terms of power spectra of intensity and phase, while spatial statistics are being obtained

[1]Now with Physical Dynamics, Inc., Bellevue, Washington 98005.

in the form of intensity and phase correlation coefficients between UHF receiving antennas spaced on baselines of a few hundred meters. Spectral coherence is being characterized by means of analogous correlation coefficients between spectral lines in the seven-line UHF spectrum.

1.2. *The DNA Wideband beacon.* The payload is a multifrequency beacon that radiates a total of ten phase-coherent RF spectral lines: one at VHF, seven at UHF, one at *L* band, and one at *S* band. All transmitted frequencies are harmonics of 11.4729 MHz, being derived from the same crystal oscillator operating at 34.4187 MHz, and the intended polarization for all frequencies is right circular. The radiated frequencies are shown in Table 1, together with the maximum effective radiated powers.

The antennas are nadir-directed; however, in an attempt at approximately uniform earth coverage, all beams except that for VHF were tailored to radiate somewhat less at beam center than toward the earth's limbs. In the case of the four highest UHF spectral lines, the beam observed after launch has a much deeper central null than intended (approaching 20 dB). Observers who may want to receive one of the UHF signals from DNA-002 are advised to select one of the three lower sidebands.

The satellite is gravity-gradient stabilized, and the orbit is sun-synchronous and highly stable. At epoch 1 January 1977, equator crossings were at 1122:43 (northward) and 2322:43 (southward) local time and were drifting later at the rate of 1.6 sec per day. This orbit was chosen as a compromise between desires for pre-midnight observations near the geomagnetic equator and post-midnight observations in Alaska.

TABLE 1. Transmission characteristics.

Designation	Frequency (MHz)	Harmonic number (of 11.4729 MHz)	ERP (dBm)
VHF	137.6748	12	+26
	378.6057	33	+27
	390.0786	34	+26
	401.5515	35	+30
UHF	413.0244	36	+27
	424.4973	37	+27
	435.9702	38	+25
	447.4431	39	+28
L band	1239.073	108	+25
S band	2891.171	252	+27

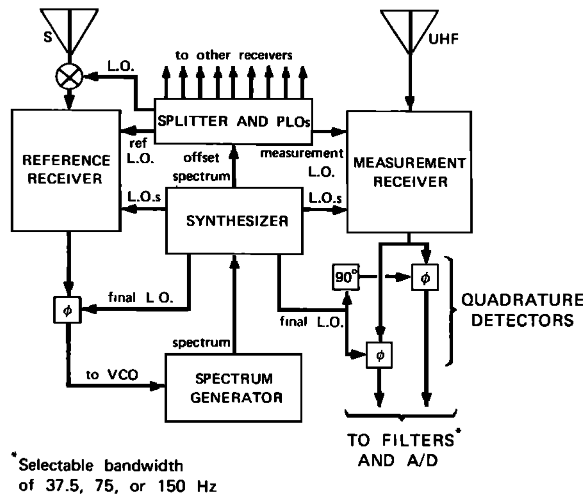

Fig. 1. Simplified block diagram of coherent receiver employed, illustrating the reference channel and one of the 9 to 12 (depending upon station configuration) measurement channels.

2. GROUND INSTRUMENTATION AND DATA HANDLING

2.1. *Coherent receivers.* The key to the experiment is to retain the coherence inherent in the transmitted signals, throughout the receiving operation on the ground. This is accomplished by means of the receiver, illustrated schematically in Figure 1. The heart of the receiver is a frequency synthesizer that is essentially a replica of the satellite-borne transmitter. The synthesizer produces a spectrum identical to that transmitted, which is then offset to provide local-oscillator signals plus other signals employed in several frequency translations.

The synthesizer is phase-locked by means of a loop operating on the output of the *S*-band reference receiver. The reference receiver chain is identical, except for the first mixer, to the various measurement receiver chains, one of which (for one of the UHF spectral lines) is illustrated in Figure 1. There is one measurement receiver channel for the VHF signal, one for the *L*-band, and one for each of the seven UHF signals. In addition, there is an identical measurement channel for each remote receiving antenna, the number of which is different at the various receiving stations.

The signal in each receiver chain finally is translated to an essentially zero-frequency baseband signal by means of two quadrature detectors. In practice, the output is at the differential Doppler

TABLE 2. Ground station locations.

Station	Geodetic coordinates of main antenna Latitude	Longitude	Geomagnetic dip latitude
Poker Flat, Alaska	65°7′34″N	147°29′14″W	65.4°N
Ancon, Peru	11°46′34″S	77°9′00″W	0.4°N
Kwajalein, Marshall Islands	9°24′08″N	167°28′10″E	4.4°N
Stanford, California	37°24′10″N	122°10′27″W	42.8°N

frequency between a specific measurement signal and the S-band reference. In the case of the remote antennas, the output frequency is the algebraic sum of the differential Doppler frequency and the relevant interferometer fringe rate. The output signal is modulated by intensity and phase scintillations.

There are three existing Wideband satellite ground stations. The first is situated just north of Fairbanks, Alaska, for studying propagation effects of the auroral ionosphere. The station is located at the University of Alaska's Poker Flat Rocket Range, near the town of Chatanika. The location was chosen to permit comparative studies with sounding rockets and existing ground-based instruments, particularly the incoherent-scatter radar at Chatanika [*Leadabrand et al.*, 1972]. The other two stations are situated for studies of equatorial scintillation. One is at the Instituto Geofisico del Peru's receiving site at Ancon (near Lima), which was chosen largely because of its location beneath the equatorial electrojet. Comparative studies are planned with the backscatter radar at Jicamarca [*Bowles*, 1963].

Initially, the third Wideband station was located at Stanford, California, for observation of the beacon signals through the relatively undisturbed midlatitude ionosphere. The Stanford station was moved to Kwajalein atoll in the Marshall Islands in September-October 1976 to provide a second equatorial station. Comparison of results from Kwajalein and Ancon will permit study of the suspected morphological differences in scintillation at different longitudes and similar geomagnetic latitudes [*Basu et al.*, 1976]. Rocket soundings of the equatorial ionosphere also are planned at Kwajalein in conjunction with Wideband passes. Station coordinates are given in Table 2.

At Poker Flat and Kwajalein, there are four receiving antennas: a 3.7-m dish that program-tracks the satellite and receives all ten signals, and three remote antennas that receive only the central UHF spectral line (413 MHz). The remote antennas are optimally directed for a specified satellite pass but do not track, relative to the main antenna; they are on geomagnetically oriented baselines of 300 m west, 600 m east, and 900 m south. At Ancon, the main (tracking) antenna is a 9.1-m dish and there is a single remote antenna 300 m east of the dish. Only a single (9.1-m, multifrequency, tracking) antenna was used at Stanford.

The receiver outputs are bandlimited in video filters that have selectable bandwidths of 150, 75, or 37.5 Hz. All operation to date has been at the maximum bandwidth on all channels. The filtered outputs are digitized on-line and are recorded magnetically under control of a station minicomputer (HP 2100 with 16k words of memory), which also controls antenna tracking and receiver tuning. To maintain maximum linearity, it is the quadrature components of each measurement signal that emerge from the receiver for recording; most data processing, however, is in terms of intensity and phase. Aside from oscilloscope and meter displays, the only real-time output is a strip chart of VHF intensity and phase, which is calculated by the computer from the VHF quadrature components. An example of the real-time records is presented in Figure 2.

The record shown in Figure 2 was obtained at Poker Flat, Alaska, on 23 November 1976, starting just after local midnight. (Local standard time at Poker Flat lags Universal Time by 10 hours.) The pass was from north to south, reaching a maximum elevation of 73° to the east of the station. The main characteristic of the pass is that it provided a clear-cut example of the subauroral scintillation boundary [*Aarons et al.*, 1969], with the effects of ionospheric irregularities evident throughout the first half of the pass but absent in the second half. The boundary is obvious upon inspection of the intensity record; it is also evident in the phase record, which reveals a smooth, slab-like ionosphere to the south but many gradients in total electron content (the line integral of electron density along the radio line of sight), or TEC [*Klobuchar*, 1973], to the north.

2.2. *Separation of scintillations from trends.* If one thinks of scintillation as arising from relatively small-scale (on the order of a kilometer) irregularities imbedded in an otherwise smooth, vertically stratified ionosphere, then one would expect a phase record to be easily separable into a smoothly varying

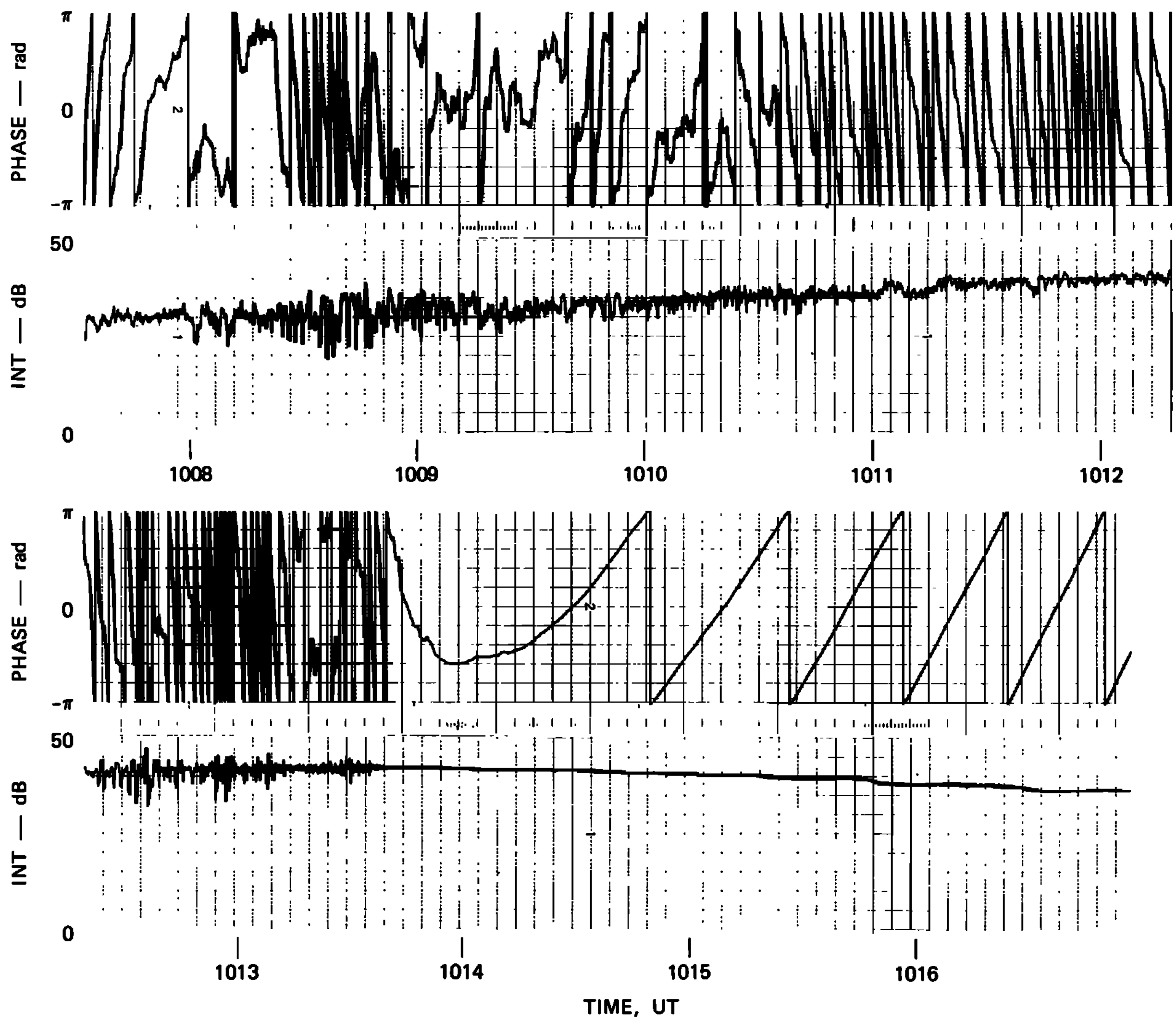

Fig. 2. Example of real-time output: strip chart of VHF (138-MHz) phase and intensity obtained at Poker Flat, Alaska, on 23 November 1976, just after local midnight (AST = UT − 10 hr). Note transition (subauroral scintillation boundary) from irregular to smooth, slab-like ionosphere as satellite line of sight scanned through about 64° N magnetic invariant latitude.

trend (caused mainly by the changing pathlength through a slab-like ionospheric layer) and relatively fast fluctuations, i.e., phase scintillations. In practice, however, it appears that, when structured, the ionosphere contains irregularities on a vast spectrum of scales extending at least from the order of a hundred meters to at least tens and maybe hundreds of kilometers [*Dyson et al.*, 1974]. A radio wave passing through such a structured plasma develops phase perturbations across the same extended spatial spectrum [*Bramley*, 1955].

Intensity scintillation, however, is a pure propagation effect arising from a combination of focusing/defocusing and diffraction pattern development, as will be discussed in section 3.2. As a consequence, the spectrum of intensity scintillations is limited at the low-frequency end by the phenomenon of Fresnel filtering [*Rufenach*, 1971]. The extended nature of the phase spectrum and the Fresnel cutoff of the intensity spectrum require that scintillation be defined on the basis of intensity.

Thus, we have chosen to regard as phase scintillations those variations that are as fast or faster than the slowest intensity scintillations and as phase trends those changes that are still slower. The spatial spectrum of the ionosphere, of course, is translated into a temporal spectrum of the signal by the scanning motion of the radio line of sight. The scan velocity in the F layer is about three kilometers per second and that in the E layer is about one kilometer per second.

In April 1975, a satellite (P72-2) carrying the first DNA Wideband beacon was lost due to a launch failure. (The beacon now operating was a backup payload.) In the intervening year before launch of the present Wideband satellite, interim observations were made of the 150-MHz and 400-MHz signals radiated for navigational purposes from a number of operational Transit satellites. On the basis of the interim data, a fluctuation period of 10 sec was established as the demarkation between "trends" and "scintillations." Specifically, it was found that removing intensity trends with Fourier periods longer than 10 sec did not appreciably alter the measured value of the S_4 [*Briggs and Parkin*, 1963] scintillation index, which is defined as the standard deviation of the received signal intensity normalized to the mean intensity.

The first data processing procedure in the Wideband satellite experiment consists of separating trends and scintillations in the following straightforward manner. First, the phase and intensity of the received signal are each smoothed by means of a low-pass, six-pole Butterworth filter with a (3-dB) cutoff at 0.1 Hz. The smoothed phase is stored as the phase trend and also is subtracted from the point-by-point phase; the residual is stored as phase scintillation. The smoothed intensity also is stored, and the raw values of intensity are divided by the intensity trend. Thus, the "detrending" process is equivalent to passing the received signal through a coherent AGC circuit.

The intensity and phase trends for the VHF record shown in Figure 2 are displayed in Figure 3. While the (dispersive) phase cannot be measured absolutely in the experiment, it is possible to obtain an estimate of the absolute starting value on a given frequency by measuring the second difference of phase among a triplet of UHF spectral lines. The second difference of phase, $\Delta_2\phi$, is obtained by forming the phase difference between a "carrier" and an "upper sideband" and again between the corresponding "lower sideband" and the same "carrier" and then taking the difference of the differences. The result is a measure of dispersion

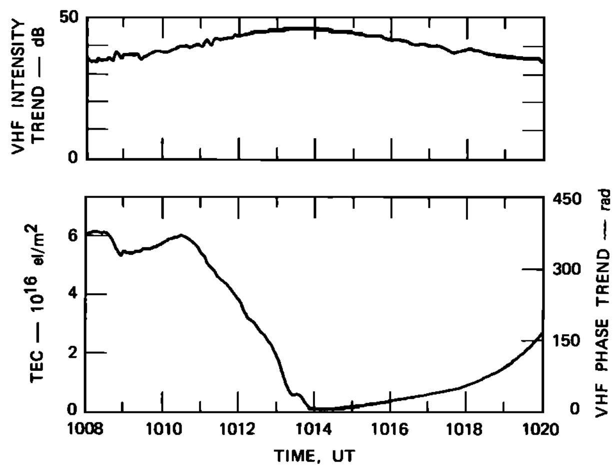

Fig. 3. Intensity and phase trends obtained from record displayed in Figure 2 by employing six-pole, Butterworth, low-pass software filters having 3-dB cutoffs at 0.1 Hz. The manifold 2π ambiguity in the starting point of phase is resolved by dispersion analysis of three UHF spectral lines.

that is related to TEC [*Burns and Fremouw*, 1970] as follows:

$$\Delta_2\phi = \frac{e^2}{2\pi\epsilon_0 mc}\frac{f_m^2}{f^3}\int_0^s N\,ds \tag{1}$$

where

e = electron charge
ϵ_0 = permittivity of free space
m = electron mass
c = speed of light
f_m = "modulation" frequency separating the spectral lines of the triad
f = "carrier" frequency (frequency of the center line of the triad)

and TEC is given by the integral of electron density, N, along the line of sight from the receiver to the satellite.

The individual dispersive phases also are proportional to TEC as follows:

$$\phi = \frac{e^2}{4\pi\epsilon_0 mcf}\int_0^s N\,ds \tag{2}$$

The frequencies of the UHF spectrum were chosen to provide a sufficiently small value of f_m that (1) can be employed to resolve the manifold ambiguity in (2). The lower part of Figure 3 contains scales for both TEC and an estimate of the absolute value of VHF dispersive phase. The plot indicates clearly that the radio line of sight encountered a transition between the auroral ionosphere (produced by charged-particle precipitation) and the relatively smooth and depleted lower-latitude ionization "trough" at about 1014 UT. That the TEC transition is also the location of the scintillation boundary is evident on careful inspection of Figure 4 (especially the phase channel), which shows the detrended phase and intensity scintillation records obtained from the pass being discussed.

The intensity-trend record in Figure 3 reveals that some intensity-scintillation energy does fall outside the passband of the 0.1-Hz detrend filter. That is, there are random fluctuations of a few dB in the "trend" during the first third, or so, of the pass. However, compared with the scintillations of up to 15 dB (peak to peak) shown in the detrended intensity record in Figure 4, the trend variations would contribute little to the intensity scintillation index.

Furthermore, careful inspection of the intensity trend in the final third of the pass reveals variations of a couple of dB with periods as short as about twenty seconds. The latter variations are thought to result from structure in the transmit-antenna pattern; use of a longer detrend cutoff would contaminate the scintillation records with such experimental artifacts. Because scintillation is bulk-processed for statistical analysis, it is beneficial to deal with such problems in the trend component, which is treated more deterministically in individual cases.

More important, it is often the case that statistical stationarity does not exist in the records for more than a few tens of seconds, which corresponds to a few times 30 km in the *F* layer and a few times 10 km in the *E* layer. This is especially true in the Alaskan records, where scintillation often is "patchy." To use a longer detrend cutoff would complicate statistical analysis considerably.

The subtleties associated with intensity scintillations slower than 0.1 Hz are confined to the VHF records because the Fresnel-filter cutoff frequency increases with decreasing radio wavelength. The very existence of such scintillations, even at VHF, is interesting because the Fresnel-zone radius, $\sqrt{\lambda z}$, for our VHF signal and satellite altitude is on the order of a kilometer in the *F* layer and a half kilometer in the *E* layer. This means that intensity scintillations with periods much longer than a second arise from focusing and defocusing in irregularities behaving as lenses. Such behavior is facilitated by the dominance of large-scale structure in the ionosphere's spatial spectrum. Again, the effect is less prominent at higher frequencies because the focal length of such lenses increases with decreasing wavelength, due to the dispersive nature of the ionosphere.

2.3. *Parameters routinely measured.* The raw-data tapes consist of time records of quadrature components from each of the receiver channels (up to 13 channel pairs), each record digitized at the rate of 500 samples per second. The raw data are retained for such purposes as high-time-resolution spectral analysis of data from events of special interest. Bulk processing, however, is done on reduced-data tapes consisting of the trends and scintillations separated as described in section 2.2. Before detrending, the data are decimated to 100 samples per second (sps). The detrended data are decimated once more to 50 sps for calculation of various signal moments, which are output in tabular and graphical form.

Because the detrending process is very time-consuming, only nine channels are detrended routinely at each station (six at Stanford), as shown in Table 3. In Table 3, capital letters stand for the frequency band; the subscripts *l*, *u*, and *c* stand for lower sideband, upper sideband, and center, respectively; *e*, *w*, and *s* stand for east, west, and south remote antenna, respectively; and numbers stand for sideband orders.

Detrended VHF strip charts, such as the sample in Figure 4, are generated in the field from each reduced-data tape. The signal moments that are output are identified (in the configuration used for Poker Flat and Kwajalein) in Table 4. In Table 4, $\hat{I}$ is a value of the intensity trend; $\hat{\phi}$ is a value of the phase trend; S_4 is the intensity-scintillation index, defined as the normalized standard deviation of intensity; σ_ϕ is a phase-scintallation index defined as the standard deviation of phase; ρ_ϕ and ρ_I are

TABLE 3. Channels contained on reduced-data tapes.

Poker Flat and Kwajalein	Ancon	Stanford
V, U_{l3}, U_{u3}	V, U_{l3}, U_{u3}	V, U_{l3}, U_{u3}
S, U_c, U_s	S, U_c, U_e	S, U_c, L
L, U_e, U_w	L, U_{l2}, U_{u2}	

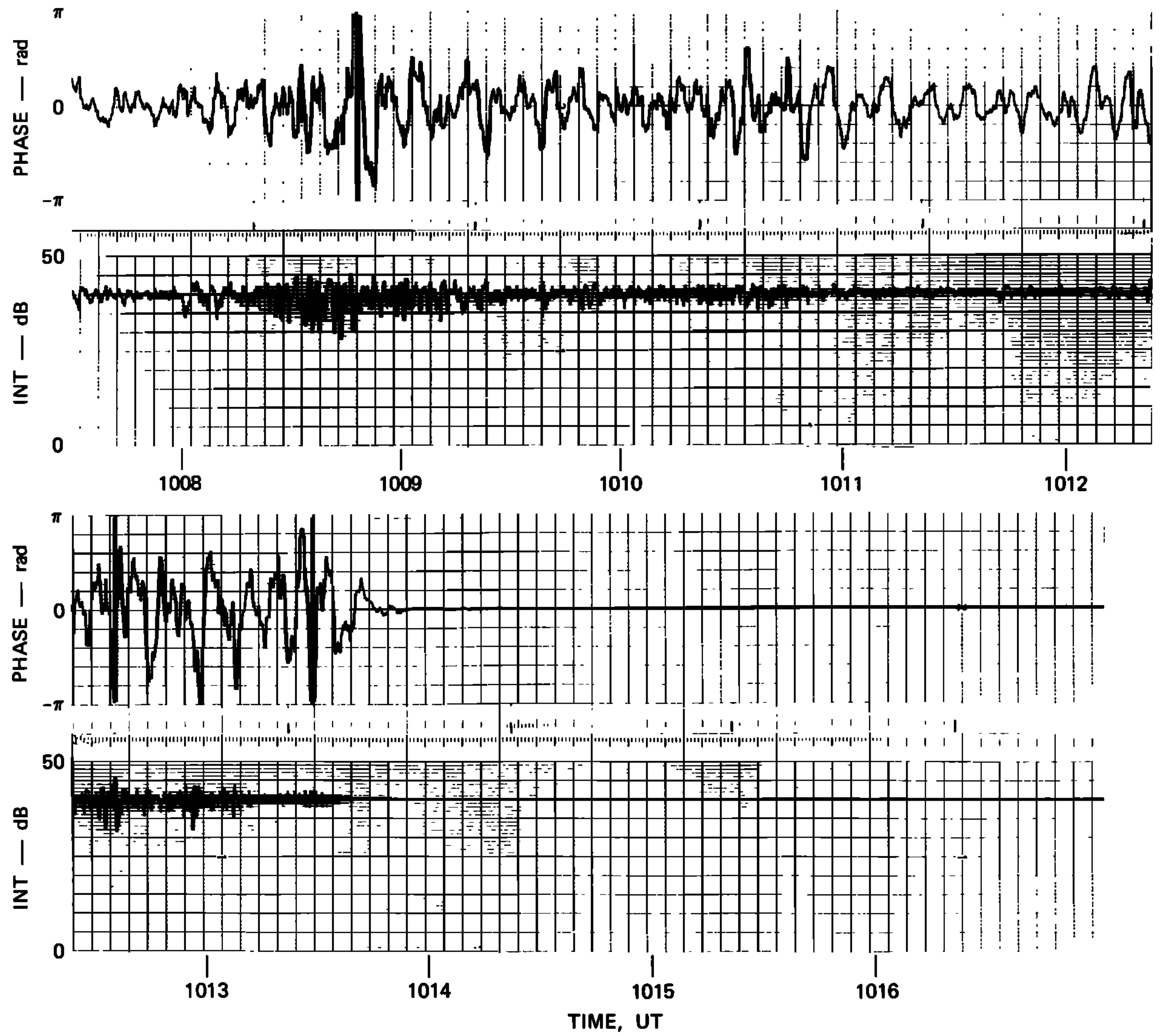

Fig. 4. VHF phase and intensity scintillations isolated from the record displayed in Figure 2 by employing the trends displayed in Figure 3 as the reference signal to a software coherent AGC processor.

correlation coefficients for phase and for intensity, respectively; $\sigma_{\delta\phi}$ is the standard deviation of phase difference.

Thus, the top three rows reveal trends and first-order, signal-statistical moments (i.e., intensity and phase scintillation indexes), while the last row contains information on second-order statistics, namely, measures of spectral coherence (between the upper and lower third UHF sidebands) and of angle scintillation and spatial coherence (between

TABLE 4. Reduced data tabular outputs (Poker Flat and Kwajalein).

$\hat{I}_V$	$\hat{\phi}_V$	$\hat{I}_{U_c}$	$\hat{\phi}_{U_c}$	$\hat{I}_L$	$\hat{\phi}_L$	S_{4V}	$\sigma_{\phi V}$	S_{4U_c}	$\sigma_{\phi U_c}$	S_{4L}	$\sigma_{\phi L}$
$\hat{I}_S$	$\hat{\phi}_S$	$\hat{I}_{U_{l3}}$	$\hat{\phi}_{U_{l3}}$	$\hat{I}_{U_{u3}}$	$\hat{\phi}_{U_{u3}}$	S_{4S}	$\sigma_{\phi S}$	$S_{4U_{l3}}$	$\sigma_{\phi U_{l3}}$	$S_{4U_{u3}}$	$\sigma_{\phi U_{u3}}$
$\hat{I}_{U_e}$	$\hat{\phi}_{U_e}$	$\hat{I}_{U_w}$	$\hat{\phi}_{U_w}$	$\hat{I}_{U_s}$	$\hat{\phi}_{U_s}$	S_{4U_e}	$\sigma_{\phi U_e}$	S_{4U_w}	$\sigma_{\phi U_w}$	S_{4U_s}	$\sigma_{\phi U_s}$
$\rho_{\phi U_3}$	ρ_{IU_3}	$\sigma_{\delta\phi U_{ew}}$	$\rho_{\phi U_{ew}}$	$\rho_{IU_{ew}}$	$\sigma_{\delta\phi U_{cs}}$	$\rho_{\phi U_{cs}}$	$\rho_{IU_{cs}}$				

the most widely spaced east-west and north-south antennas). Each of the entries in Table 4 represents a column of data, with one value output for each 20-sec segment of a pass. Each data row is preceded by marks of time, azimuth, and elevation.

Explicit definitions of the scintillation indexes and correlation coefficients obtained are given in (3) through (7), where I and ϕ are understood to represent detrended values of intensity (amplitude squared) and phase, respectively, and $\langle\,\rangle$ represents a temporal average over 20 sec.

$$S_4^2 = (\langle I^2 \rangle - \langle I \rangle^2)/\langle I \rangle^2 \tag{3}$$

$$\sigma_\phi^2 = \langle \phi^2 \rangle - \langle \phi \rangle^2 \tag{4}$$

$$\sigma_{\delta\phi_{ab}}^2 = \langle (\phi_a - \phi_b)^2 \rangle - \langle (\phi_a - \phi_b) \rangle^2 \tag{5}$$

$$\rho_{I_{ab}}^2 = \langle I_a I_b \rangle / (\langle I_a^2 \rangle \langle I_b^2 \rangle)^{1/2} \tag{6}$$

$$\rho_{\phi_{ab}}^2 = \langle (\phi_a - \langle \phi_a \rangle)(\phi_b - \langle \phi_b \rangle) \rangle / \sigma_{\phi_a} \sigma_{\phi_b} \tag{7}$$

In addition to the above signal moments, a dB fade index is computed for VHF, UHF, and L band. It is defined as the (negative) dB excursion (relative to the established trend level) of the 98th percentile point during the 20-sec interval, calculated from a sample population of 2000 points (i.e., from a record having 100 samples per second).

It will be noted that the definition of correlation coefficient used for intensity is different from that used for phase. The definition given in (6), in which the mean is not subtracted, is preferable in the inevitable presence of system noise; in the absence of scintillation, it takes on a value extremely close to unity. The coefficient defined in (7), however, reduces to a small value in the absence of scintillation because system noise is uncorrelated in different receiver channels. The mean value of phase is effectively removed in the detrending process, however, and there is no steady value of phase analogous to the long-term mean received signal intensity. As a consequence, the zero-mean definition of correlation coefficient is used for phase, out of necessity; it is a meaningful parameter whenever significant phase scintillation is present.

3. SOME EARLY RESULTS

3.1. *Types and severity of complex-signal scintillation.* Wideband is the first coherent beacon to provide an essentially undisturbed phase reference and therefore to permit a full and reliable characterization of the complex-signal statistics associated with scintillation. Consequently, even a cursory scanning through detrended strip charts such as the one appearing in Figure 4 is instructive in revealing recognizable types of complex-signal scintillation. Examples of some recurring types are presented in Figure 5.

By far the most common type is that termed "classical" scintillation, which consists of relatively rapid variations in received signal intensity and slower phase variations, both highly random in nature. Classical scintillation usually occurs in intervals of a few minutes during a pass, corresponding to fields of ionospheric structure having north-south extents of several hundred km. Similar behavior occurring over a shorter interval, on the order of a minute or less, corresponding to a patch of less than a couple hundred km in north-south extent, is referred to as a "classical patch." Classical patches abound on passes over Poker Flat and are seen less frequently at the lower-latitude stations. We have found recently that there often is a prominent classical patch of enhanced scintillation located at the boundary between the auroral ionosphere and the lower-latitude trough.

Another type of very random intensity and phase fluctuation that has been observed a number of times, mainly at the lower-latitude stations, is termed "classical slow" scintillation because the intensity variations appear slower to the eye on strip charts than do classical intensity scintillations. Another characteristic of classical slow scintillation is that the phase variance associated with a given level of intensity variation appears to be smaller than for classical scintillation. In contrast, occasional occurrences of strong phase variations in the virtual absence of amplitude fluctuation have been noted, prompting the term "phase sans amplitude" scintillation.

In addition to the various types of random scintillation, Figure 5 contains examples of more isolated and distinctive signal fluctuations. First, when scanning a record of essentially random scintillations, in a few instances one's eye is caught by a particularly sudden phase change that presumably corresponds to a "sharp phase gradient" in the wavefront arriving at the ground. Such a feature may be accompanied by an associated amplitude diffraction pattern. Finally, still more isolated or "discrete" phase variations and corresponding diffraction or focus/defocus patterns occur, especially in midlatitude records.

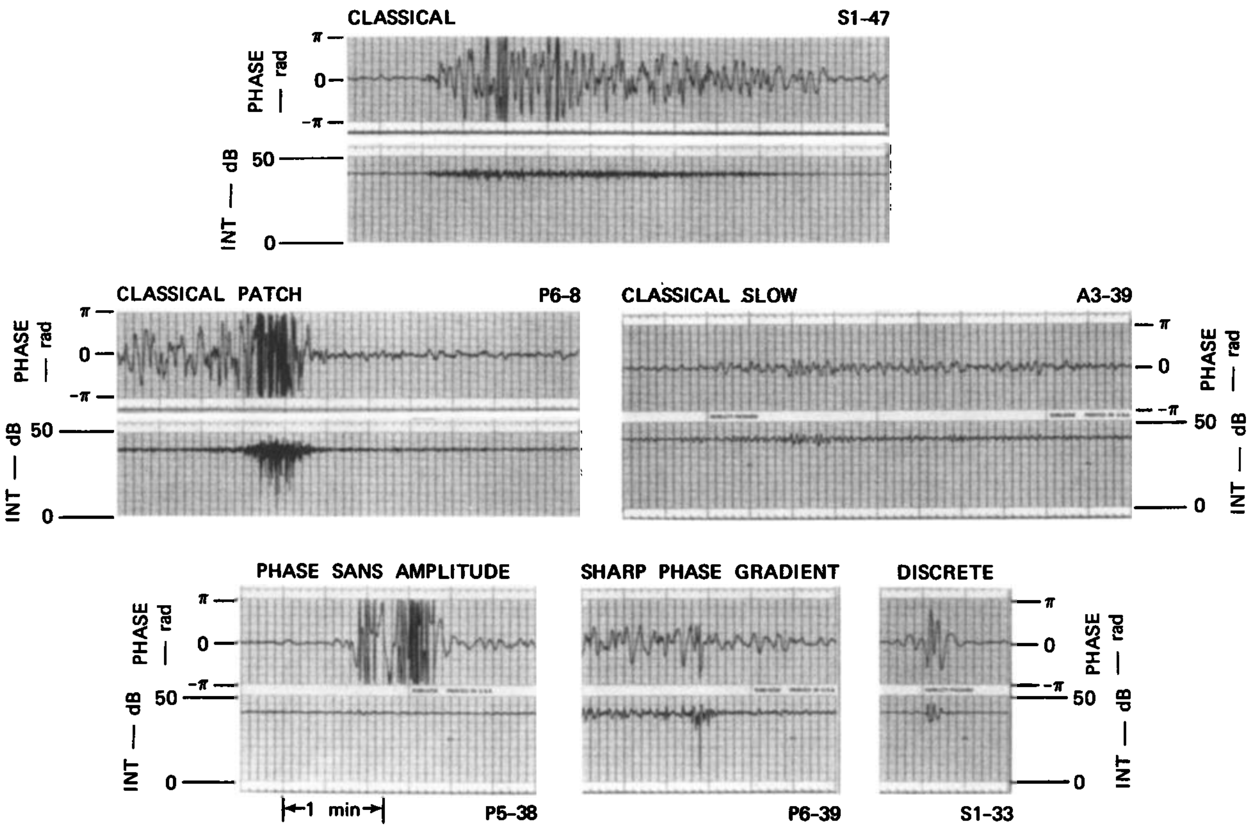

Fig. 5. Recurring types of (VHF) scintillation. By far the most common type is "classical" scintillation, including the subtype called "classical patch." The letter preceding the pass identification number at the upper right of each record strip denotes the station: S, Stanford, P, Poker Flat; A, Ancon.

While it is intended to study scintillation morphology systematically in terms of the signal moments—especially the phase scintillation index—defined in section 2.3, a visual inspection scale of (intensity and phase) scintillation level has been established as a means for quickly obtaining an overview of scintillation activity at the various stations. The overview is provided by scanning the detrended VHF strip charts to determine the severity and extent of intensity and phase scintillation, by comparison with records selected as archetypes of seven activity levels ranging from "extremely quiet" to "extremely active." Figure 6 illustrates the archetypes that define the extremes and middle of the seven-level activity scale.

To give some initial indication of the level of complex-signal scintillation observed over a period of about five months (June through October 1976) in the present epoch of minimal solar activity, Figure 7 shows the record count by activity level and ground station for passes inspected thus far. Note that the Stanford data base is from the end of May to early September only and that the Kwajalein data base is primarily from the month of October.

It is interesting to note that only the equatorial stations have yet reported either extreme of activity. It is well-known that extreme scintillation activity is encountered near the geomagnetic equator [*Skinner et al.*, 1971]. It is rather remarkable to encounter records from the same region that imply an ionospheric smoothness on the order of one electrical degree at VHF (i.e., on the order of a centimeter or less for horizontal distances up to 10 km or more) at night as well as in the daytime.

3.2. *Signal statistics of classical scintillation—First-order statistics.* Since the majority of scintillation is of the type termed classical (and its subtype, classical patch), it is this type that is most

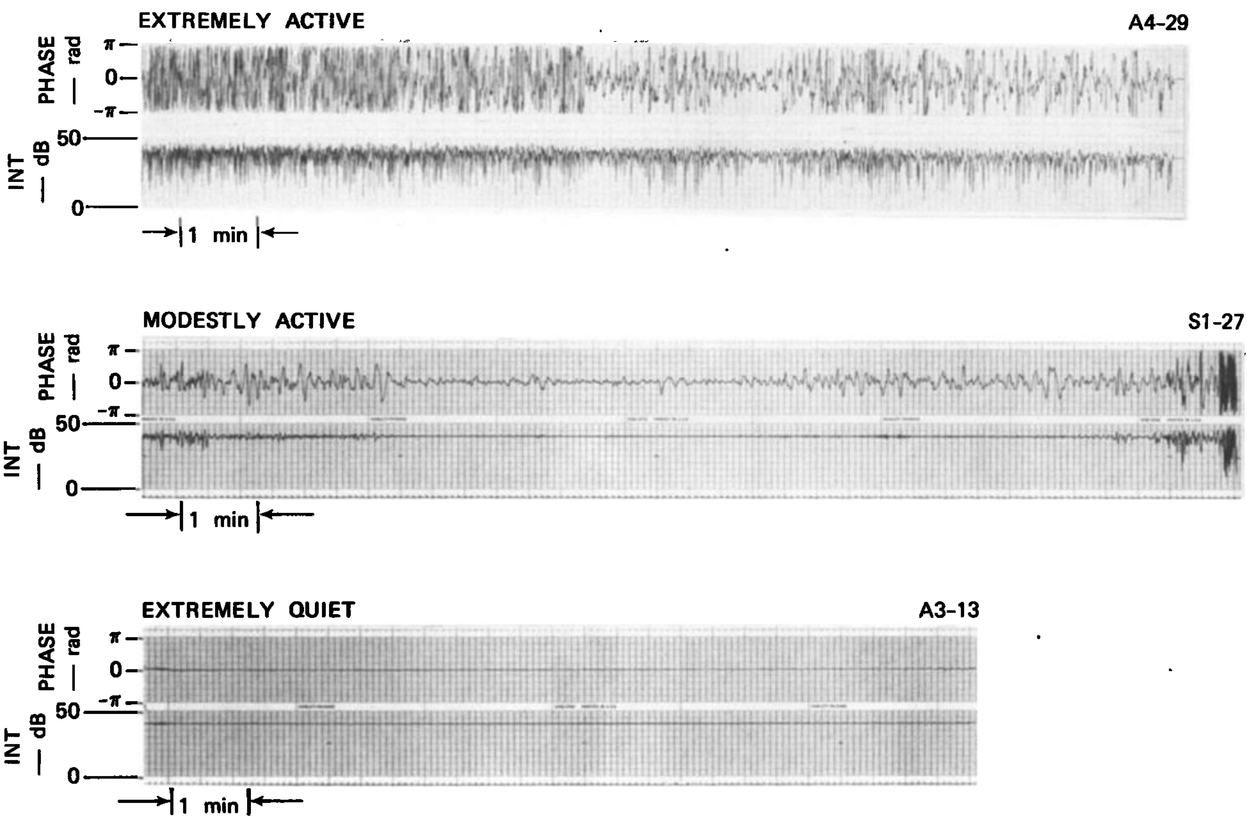

Fig. 6. Detrended VHF records chosen as typical to define the extremes and middle of a seven-level scale for quick determination of the combined severity and extent of complex-signal scintillation.

important to characterize signal-statistically from the point of view of modeling the transionospheric communication channel. Perhaps the most useful engineering information to be gleaned centers around the frequency dependence of scintillation. As an example of frequency behavior, Figure 8 displays detrended strip charts of intensity and phase obtained from a pass over Poker Flat that was categorized as very active on the basis of visual inspection of the VHF record. The same features are notable at VHF, UHF, and L band, ranging from fades as deep as 40 dB and phase excursions of several π at VHF to barely discernible intensity scintillations (a couple of dB) and phase scintillations of less than $\pm\pi$ at L band.

The intensity and phase scintillation indexes measured during this pass are shown in Figures 9 and 10, respectively. Again, the same features are identifiable on the VHF, UHF, and L band frequencies. Indeed, the standard deviations of phase track each other remarkably consistently. The intensity scintillation indexes exhibit somewhat more variability from frequency to frequency.

The same characteristics carry over to the frequency dependences of S_4 and σ_ϕ, which are illustrated (respectively) in Figures 11 and 12 for two selected 20-sec intervals. The S_4 values display a moderate amount of scatter about an $f^{-1.5}$ dependence. They also exhibit a "saturation" as the curves approach the limiting value of unity that one would expect if "fully developed" intensity scintillation obeys a Rayleigh distribution of amplitude.

In comparison with S_4, the values of σ_ϕ exhibit a remarkably ordered frequency dependence. The only departures from a strict f^{-1} dependence shown by the raw data points occur at L band, and these departures are entirely instrumental effects stemming from phase scintillation of the S-band reference signal.

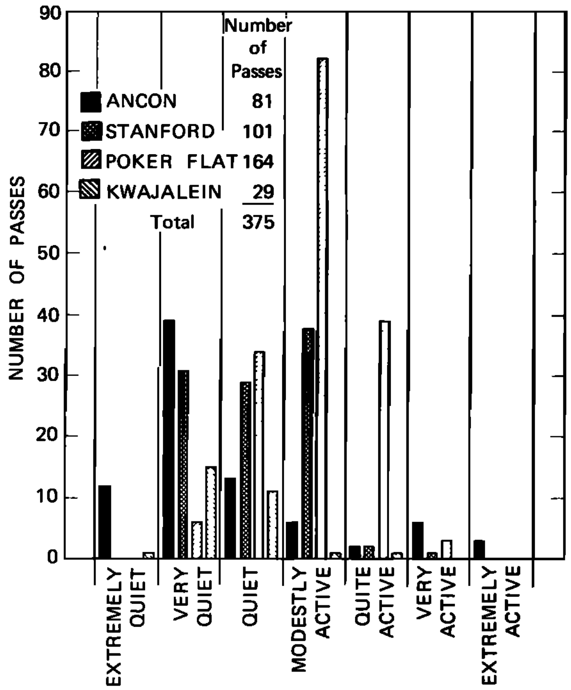

Fig. 7. Pass activity level for records inspected as of 9 December 1976. Recorded between the end of May and the end of October (Stanford to mid-September only; Kwajalein mainly during the month of October).

For refractive-index irregularities of sufficiently large scale that propagation effects within the ionospheric scattering layer itself may be ignored, the phase at each point on the output plane is given by (2). Taking the standard deviation of ϕ across that plane would result in an f^{-1} dependence for σ_ϕ. As an intensity diffraction pattern develops in post-scattering propagation (preferentially at lower frequencies), one might expect disruption of the f^{-1} frequency dependence of phase scintillation (with σ_ϕ being decreased at the lower frequencies). Figure 12 shows no such disruption.

The phase, ϕ_m, measured at the output of the coherent receiver is derived from the measurement frequency's true phase, ϕ, and that of the reference frequency, ϕ_r, as

$$\phi_m = \phi - \phi_r/n \tag{8}$$

where n is the ratio of the reference frequency to the measurement frequency. Given an f^{-1} dependence of phase scintillation and correlation between the fluctuations on the measurement and reference channels, the measured standard deviation will be related to the true standard deviation as

$$\sigma_{\phi_m} = \sigma_\phi(1 - n^{-2}) \tag{9}$$

Inverting (9) and applying it to the raw data points in Figure 12 results in a negligible change at all frequencies except L band, for which the resulting correction is shown by the square data point.

Thus, Figure 12 implies: (a) that diffraction did not change the frequency dependence of phase scintillation from that expected in the near zone of a phase-perturbing screen, and (b) that there were phase scintillations on the S-band reference channel that were correlated with those observed at L band. Both of these conclusions are consistent with production of phase scintillation by ionospheric structure having a spatial spectrum dominated by large-scale irregularities, to which we shall return in section 3.3.

Durability of phase statistics in the presence of diffraction does not necessarily mean that the spatial pattern of phase itself is not changed. Furthermore, diffraction sufficiently strong to perturb the f^{-1} dependence of σ_ϕ has been encountered. An example is presented in Figure 13, which shows the frequency dependence of phase scintillation during two 20-sec periods of a pass over Ancon shortly before local midnight. (Local standard time at Ancon lags UT by 5 hours.) In the less disturbed of the two periods, the L-band and UHF data points show the same ordered dependence noted in Figure 12, but the VHF point falls beneath the f^{-1} curve. In the more disturbed period, the VHF point is still more depressed and the UHF points display some scatter. (In all cases, the phase-screen theoretical dependence has been passed through the central UHF point.)

If phase fluctuations on a measurement channel and those on the reference channel are uncorrelated, then their variances add. The result is that, for an inherent f^{-q} frequency dependence of scintillation, the measured standard deviation in the presence of an uncorrelated reference is related to the true standard deviation as

$$\sigma_{\phi_m} = \sigma_\phi[1 + n^{-2(1+q)}]^{1/2} \tag{10}$$

In spite of the point scatter in the more disturbed data set in Figure 13, there is little doubt that the underlying frequency dependence in the UHF to L-band regime is close to f^{-1}. Thus, the correction

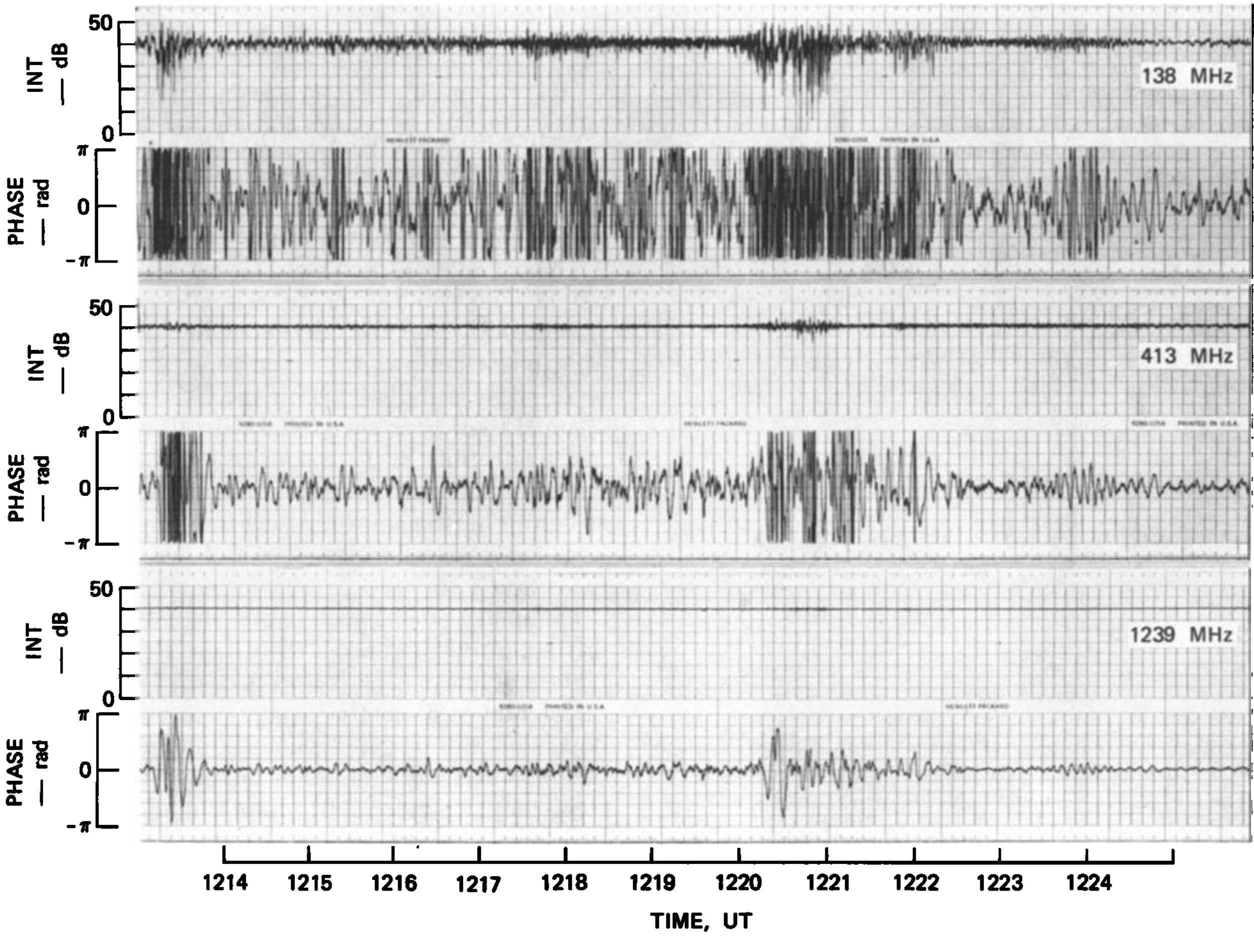

Fig. 8. Detrended VHF, UHF, and L-band strip charts from a pass recorded at Poker Flat on 29 May 1976.

needed to account for the effect of reference-phase fluctuations on the measured L-band phase is bracketed by (9) and (10) with $q \approx 1$; the vertical bar through the L-band point represents the range of uncertainty caused by reference-phase fluctuations.

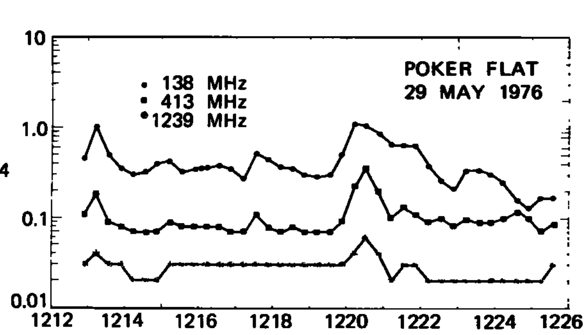

Fig. 9. Intensity scintillation indexes measured at VHF, UHF, and L-band during the pass displayed in Figure 8.

There is only a 3% difference between the raw data point and the bottom of the uncertainty range (uncorrelated condition). Drawing an f^{-1} line through the raw L-band data point would, in fact, result in a rather satisfactory fit to the cluster of UHF points. Thus, it seems likely that there were S-band fluctuations (of a little over 20° rms) during this observation that were largely uncorrelated with the L-band phase scintillations. The remaining uncertainty about the correlation and the L-band uncertainty bar in Figure 13 represent fundamental limits of the experiment, stemming from the differential nature of the phase measurement.

The intensity measurement, of course, is not differential in nature. The frequency dependence

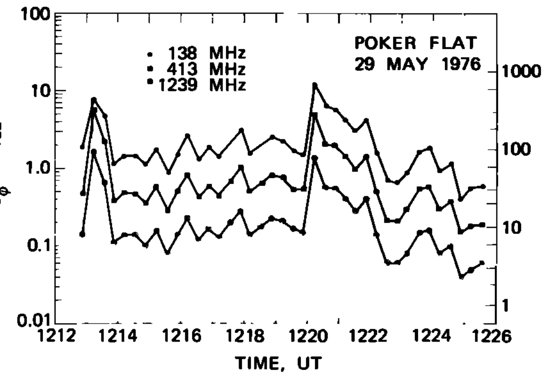

Fig. 10. Phase scintillation indexes measured at VHF, UHF, and *L*-band during the pass displayed in Figure 8.

of intensity scintillation observed during the same two periods discussed in conjunction with Figure 13 is shown in Figure 14. The "fully developed" nature of the intensity scintillation at VHF and the five UHF frequencies analyzed, during the more disturbed period, is apparent in the departure of those six data points from the $f^{-1.5}$ dependence that holds between *S* band and *L* band. An interesting point in the less disturbed period is the fact than an S_4 value of 1.20 was measured at VHF. This is the largest value noted in records inspected to date, and it is 20% larger than the limiting value

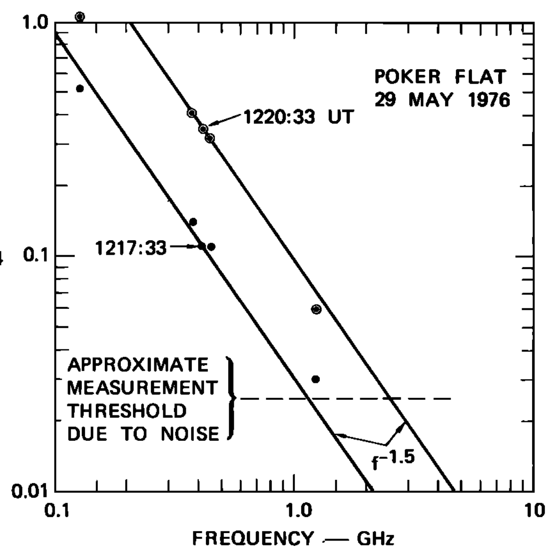

Fig. 11. Frequency dependence of intensity-scintillation index during two 20-sec periods (starting at the times noted) of the pass displayed in Figure 8, compared with an $f^{-1.5}$ dependence.

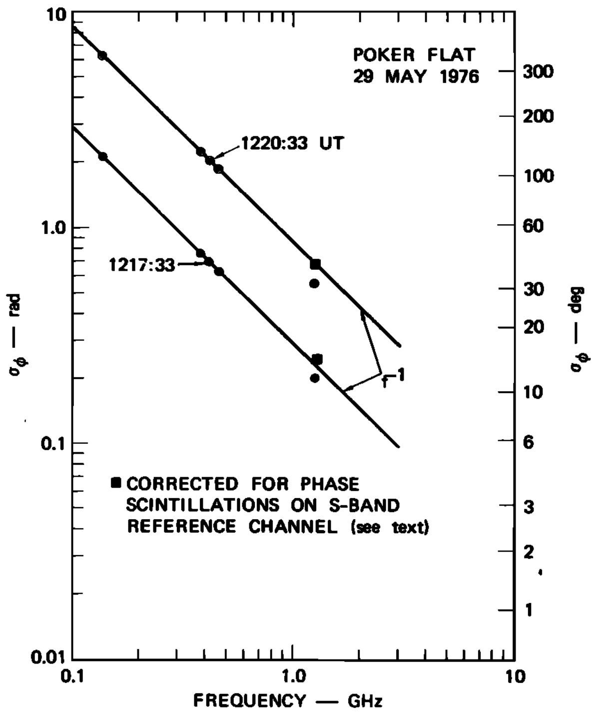

Fir. 12. Frequency dependence of phase-scintillation index, during two 20-sec periods of the pass displayed in Figure 8, compared with an f^{-1} dependence.

predicted for a Rayleigh distribution of amplitude. Careful inspection of the VHF time record for this 20-sec period reveals three prominent signal enhancements and one very deep fade which suggests focus effects caused by particular ionospheric ir-

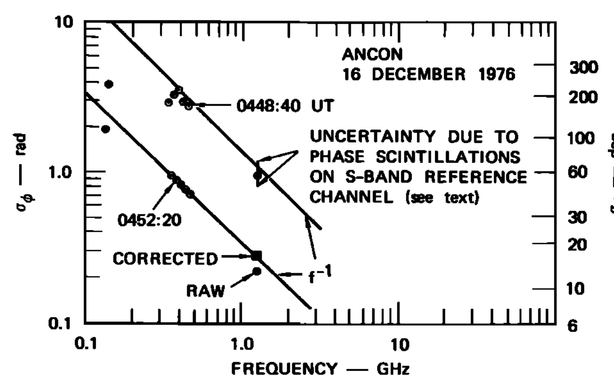

Fig. 13. Frequency dependence of phase-scintillation index during two 20-sec periods of pass recorded at Ancon on 16 December 1976, compared with an f^{-1} dependence arbitrarily passed through the 413-MHz data point.

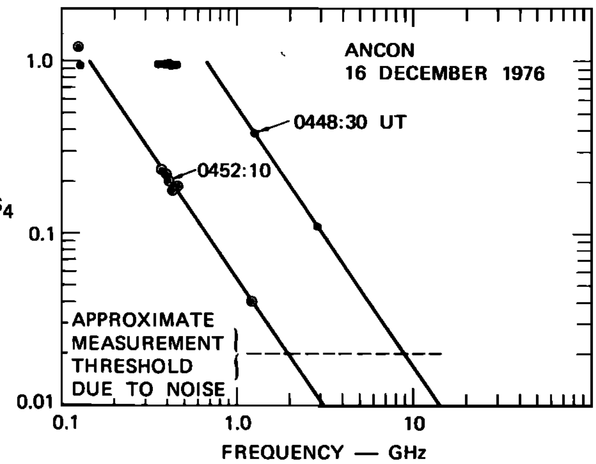

Fig. 14. Frequency dependence of intensity-scintillation index during two 20-sec periods of the pass partially displayed in Figure 23, compared with an $f^{-1.5}$ dependence.

regularities that may have dominated the signal behavior during this short time interval.

More detailed analysis of first-order signal statistics has suggested to us the presence of a focus component as an integral part of ionospheric scintillation. Following loss of the first Wideband beacon, some complex-plane scatter plots were made of the VHF signal received from operational Transit satellites, using the coherent UHF signal as a phase reference. The scatter diagram obtained after removal of phase and intensity trends with Fourier periods greater than 10 sec was basically arc-like because of domination by phase fluctuations. Without knowing whether the (UHF) reference phase fluctuations were correlated with the (VHF) measurement-channel fluctuations, it was not possible to know in detail the effect of the former on the recovered scatter diagram. However, there was clear evidence of correlation between phase and intensity.

Successful launch of Wideband, with its much higher reference frequency, now permits a definitive look at the complex-signal statistics associated with scintillation. Figure 15 illustrates the nature of the VHF complex-signal statistics obtained during a 90-sec interval of the "classical scintillation" record shown at the top of Figure 5. For even a modest intensity scintillation index of 0.28, some of the associated phase variations (having Fourier periods of 10 sec and less for a 1000-km orbit) exceed $\pm\pi$.

That even the slow complex-signal scintillations are not pure phase variations, however, is illustrated in Figure 16, where phase and intensity fluctuations having Fourier periods between 2.5 and 10 sec have been isolated by means of the first step in a second "detrending" procedure, in which a low-pass filter having a very sharp cutoff has been employed. The signal shown in Figure 16 is the reference signal applied in the coherent AGC operation that constitutes the final step of the second detrending procedure.

The scatter diagram at the top of Figure 16 shows clear evidence of signal enhancements and fades

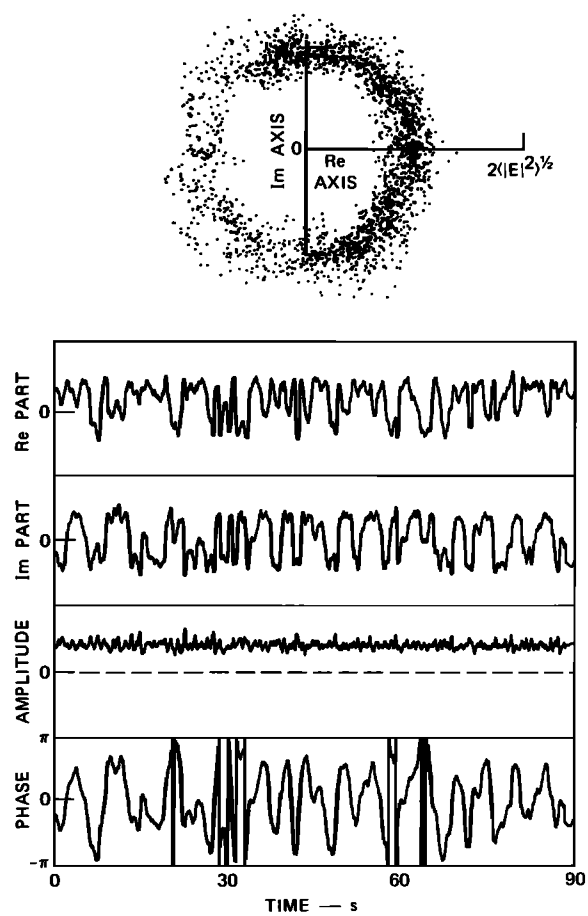

Fig. 15. Three representations of VHF complex-signal fluctuations during 90 sec of the "classical" scintillation record appearing at the top of Figure 5. Top to bottom: scatter plot on the complex plane; real and imaginary parts of the complex signal; amplitude and phase of the complex signal. This data segment was selected by eye as displaying reasonable statistical stationarity; the average intensity and phase scintillation indexes for the segment are, respectively, $S_4 = 0.28$ and $\sigma_\phi = 1.58$ rad.

on time scales comparable to the slowest phase variations retained in the first detrending procedure (i.e., those with periods between 2.5 and 10 sec). Furthermore, the intensity scintillations are correlated with the phase scintillations. That is, a phase advance is accompanied preferentially by a weak fade, and a phase retardation is accompanied preferentially by a weak signal enhancement; this is precisely the behavior that would be expected because of focusing and defocusing in the near zone of a phase-perturbing irregular ionosphere.

The signal residual of the second detrending procedure (i.e., the output of the second coherent AGC operation) is illustrated in Figure 17. The elliptical cluster of points is consistent with the generalized gaussian signal statistics [*Rino and Fremouw*, 1973] that might be expected in the intermediate zone of a phase-perturbing screen, in which the diffraction fields from several irregularities comparable in size to and smaller than the Fresnel zone are contributing to the complex-field fluctuations. The observed tilt of the ellipse arises from correlation between the quadrature components of the received signal.

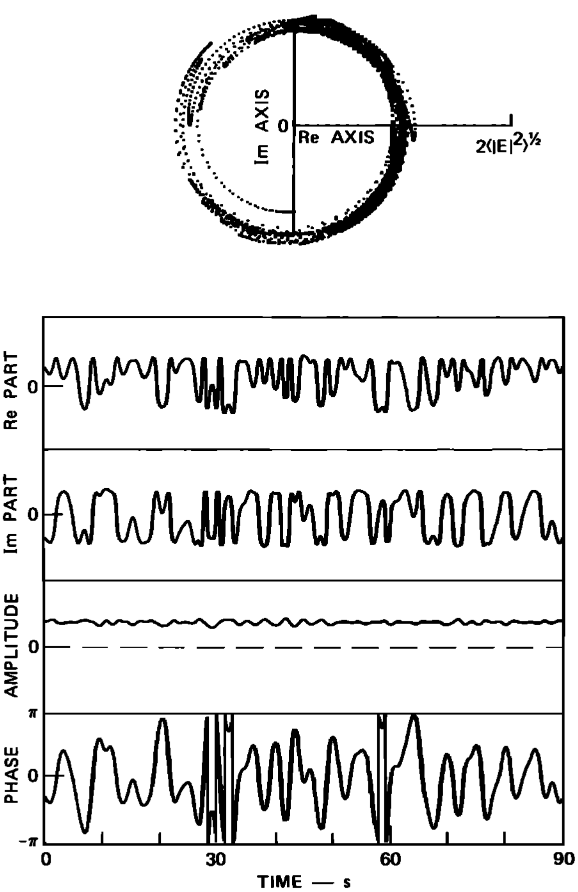

Fig. 16. The focus component (containing intensity and phase fluctuations with Fourier periods between 2.5 and 10 sec) of the scintillating signal shown at the top of Figure 5, isolated by applying a 10-pole, Butterworth, low-pass filter to the intensity and phase of the signal shown in Figure 15.

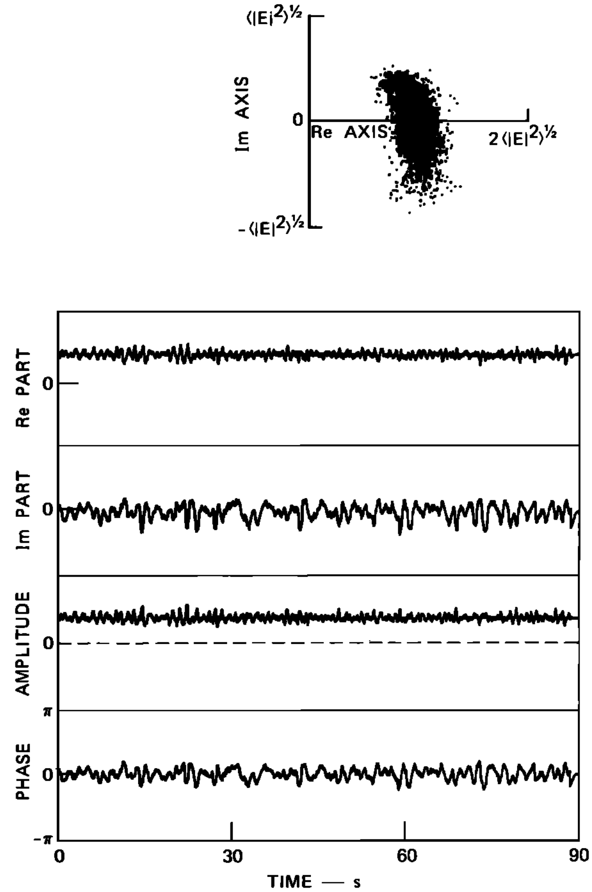

Fig. 17. The scatter component (containing intensity and phase fluctuations with Fourier periods shorter than 2.5 sec) of the scintillating signal shown at the top of Figure 5, isolated by employing the signal shown in Figure 16 as the coherent-AGC reference in a second detrending of the data shown in Figure 15.

Experimental isolation of the signal components illustrated in Figures 16 and 17 prompts us to postulate that the first-order signal statistics of scintillation can be characterized by the following two-component model:

$$E = E_s E_f = (x_s + iy_s)\exp(\chi_f + i\phi_f) \tag{11}$$

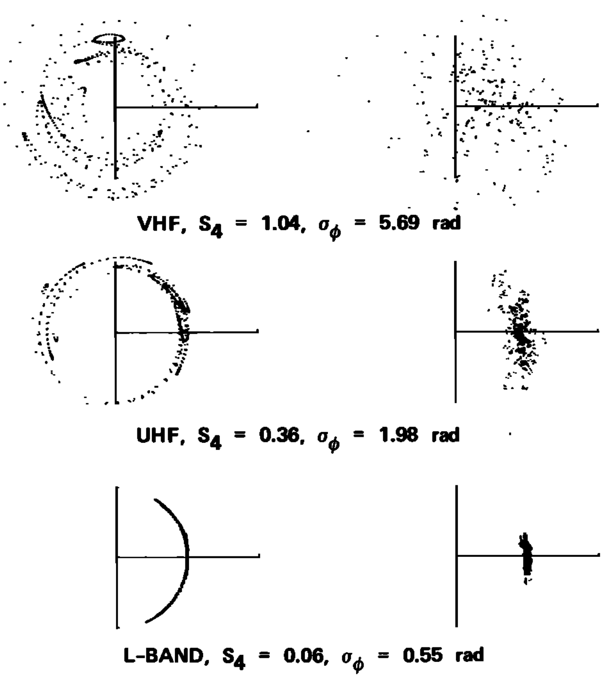

Fig. 18. Scatter diagrams of the focus (left) and scatter (right) components derived from the VHF (top), UHF (center), and L-band (bottom) records obtained during 20 sec (starting at 1220:33 UT) of the pass displayed in Figure 8.

where x_s and y_s are jointly gaussian variates, as are χ_f and ϕ_f, and where E_s and E_f are statistically independent (by virtue of the sharp second-detrend filter). We suppose E_s to arise from diffractive scatter by irregularities comparable to and smaller than the first Fresnel zone and E_f to arise from refractive focusing and defocusing by larger-scale irregularities acting as lenses. If statistical hypothesis testing proves out the above model, then it will be possible to fully characterize the first-order, complex-signal statistics of classical scintillation in terms of the "six sigmas,"

$$\sigma_{x_s}, \sigma_{y_s}, \sigma_{x_s y_s}, \sigma_{\chi_f}, \sigma_{\phi_f}, \sigma_{\chi_f \phi_f}$$

which are the (co)variances of the subscripted variables.

Preliminary indications of the durability of the two-component scintillation model are contained in Figures 18 and 19. Figure 18 shows scatter diagrams of the focus and scatter components recorded at VHF, UHF, and L band during 20 sec of a pass over Poker Flat under conditions of strong VHF scintillation. There are trends in both the focus and scatter components that, at least qualitatively, are understandable in terms of propagation theory. First, the level of perturbation in both components shows the expected strong dependence on frequency. Second, the scatter component shows a trend from near-zone (highly non-Ricean) to far-zone (Ricean) behavior as the frequency is decreased (i.e., as the Fresnel-zone size is increased).

Finally, the focus component displays an orderly trend from essentially complete dominance by phase fluctuations at L band, through development of weak focuses and defocuses correlated with the phase perturbations at UHF, to a condition that may represent a kind of statistical "focal plane" behavior at VHF. The composite VHF scintillating signal probably approximates that propagated through a Rayleigh fading channel, although systematic goodness-of-fit tests have not yet been made.

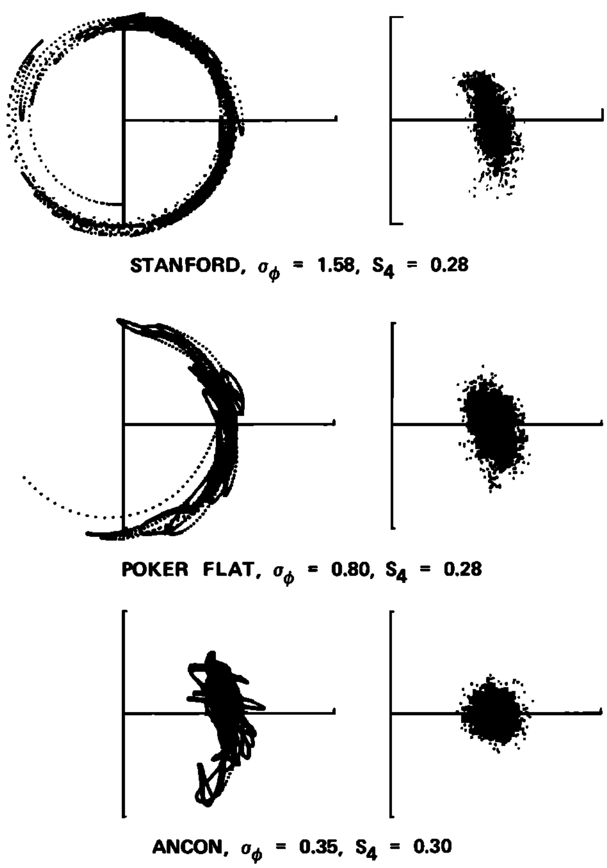

Fig. 19. Scatter diagrams for the focus (left) and scatter (right) components isolated from segments of VHF records obtained at a midlatitude (top), auroral (center), and equatorial (bottom) station.

Figure 19 contains one VHF data set from each of the three latitudinal regions being probed by means of the Wideband experiment, selected for their similar intensity scintillation indexes. A striking feature of the three data sets is that while they all exhibit an S_4 index of approximately 0.3, the standard deviation of phase ranges from 0.35 to 1.58 rad. Correspondingly, the focus and scatter components, respectively, display internally consistent trends from near- and intermediate-zone behavior to intermediate- and far-zone behavior. For instance, the equatorial (Ancon) scatter component displays a very Ricean characteristic, while that obtained at midlatitude (Stanford) is highly non-Ricean.

Figure 19 is suggestive of a latitudinal trend in the signal-statistical nature of scintillation, which may be significant both geophysically and for communication channel modeling. It is consistent, for instance, with the possibility that equatorial scintillation is produced by irregularities having a greater mean, or centroid, height than those at higher latitudes. It is premature to draw such a conclusion, however, until many more data sets are analyzed and until geometrical factors are taken into account.

3.3. *Signal statistics of classical scintillation—*

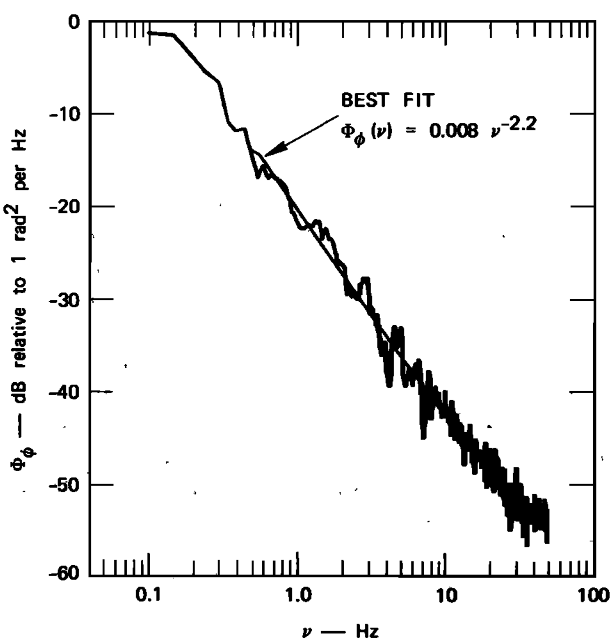

Fig. 20. Power spectrum of VHF phase for a 10 sec portion of Poker Flat pass 7-35, 27 August 1976, 1244 UT.

Second-order statistics. The time structure of radio-wave scintillation data contains information that can potentially reveal both the location and size distribution of the irregularities in the transmission medium. Intensity records alone, however, provide only limited information. As noted in section 2.2, the Fresnel filtering effect suppresses the contribution of large-scale structures. Moreover, the intensity scintillation level varies with changing irregularity strength as well as with distance from the receiver.

By measuring the full complex-signal structure, the irregularity size distribution can be determined essentially undistorted by diffraction effects. Indeed, our phase-scintillation data show no measurable Fresnel-radius dependence except for the most severely disturbed passes. This is indicated, in terms of first-order statistics, by the fact that the signal-phase variance varies quadratically with wavelength through substantial changes in Fresnel radius and scintillation level, as described in section 3.2.

It is also suggested, in second-order statistical terms, by the fact that our measured phase spectra generally show a power-law form over the medium frequency range, which is unaffected by our phase detrending operation and the noise floor.

To characterize the phase spectrum, we use a log-linear, least-squares fitting procedure to determine the strength and slope parameters, T and p respectively, defined such that

$$\Phi_\phi(\nu) = T\nu^{-p} \tag{12}$$

The fitting is done over the frequency range 0.5 Hz $\leq \nu \leq$ 10 Hz. The (3-dB) detrender cutoff is 0.1 Hz. An example is shown in Figure 20, where $T = 0.008$ and $p = 2.2$.

From (2) it follows that if the correlation distance of N along s is small compared to the path length in the irregular ionospheric layer, then

$$\varphi_\phi(\vec{\kappa}) = r_e^2 \lambda^2 L \sec\theta\, \varphi_{\Delta N_e}(\vec{\kappa}, 0) \tag{13}$$

where $\varphi(\vec{\kappa})$ denotes the spatial wavenumber spectrum, L is the layer thickness, and θ is the incidence angle of the propagation vector on the layer. If the satellite scan is along the x axis of the coordinate system, one can show that

$$\Phi_\phi(\nu) = r_e^2 \lambda^2 L \sec\theta \frac{2\pi}{v_x} \int \varphi_{\Delta N}(2\pi\nu/v_x, \kappa_y, 0) \frac{d\kappa_y}{2\pi} \tag{14}$$

By comparison, a one-dimensional, *in situ* probe would measure the power spectrum

$$\Phi_{\Delta N}(\nu) = \frac{2\pi}{v_x} \int\int \varphi_{\Delta N}(2\pi\nu/v_x, \kappa_y, \kappa_z) \frac{d\kappa_y}{2\pi} \frac{d\kappa_z}{2\pi} \qquad (15)$$

The form $\Phi_{\Delta N}(\nu)$ that corresponds to (12) is $\Phi_{\Delta N}(\nu) = T\nu^{-(p-1)}$.

From our preliminary data analysis, we believe that the spectrum shown in Figure 20 is typical of the phase scintillation accompanying weak intensity scintillation, although the spectral index is, in general, highly variable. We have observed p values in the range $2 < p < 4$. *Phelps and Sagalyn* [1976] have reported a similar variation in measured *in situ* spectra with index values for weak irregularities less than 2 ($p = 3$) and values approaching or exceeding 2 for stronger irregularities ($p > 3$). The strength parameter, T, is numerically equal to the power spectral density of phase at a fluctuation rate of 1 Hz. Unlike the phase variance, T is unaffected by detrending.

For the intensity spectra, we have derived a measure of the intensity scintillation rate by estimating the diffraction-induced turnover at the low-frequency end of the spectrum. The estimate is implemented by logarithmic, least-squares fitting

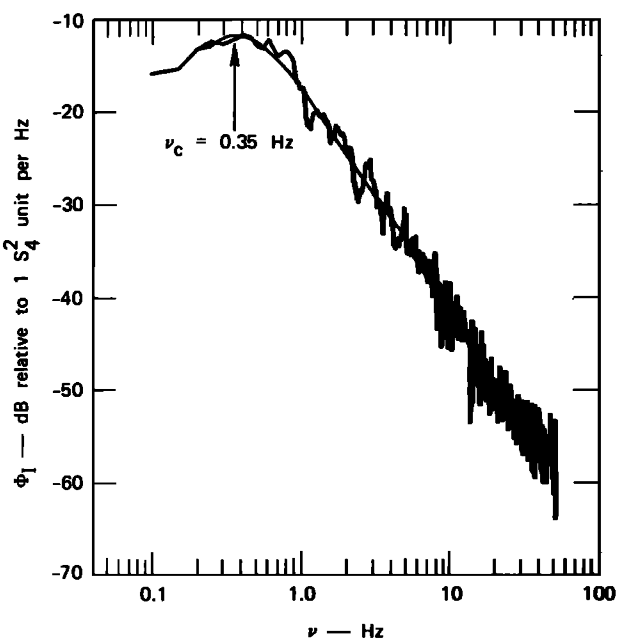

Fig. 21. Power spectrum of VHF intensity for a 10 sec portion of Poker Flat pass 7-35, 27 August 1976, 1244 UT.

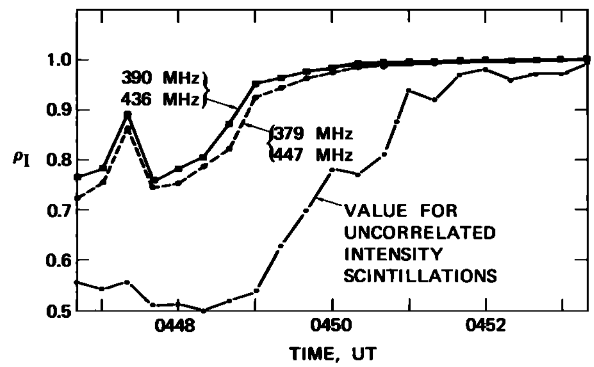

Fig. 22. Spectral decorrelation behavior of UHF intensity during portion of pass recorded at Ancon on 16 December 1976. (Data points placed at centers of 20-sec calculation intervals.)

of a cubic function to the intensity spectrum between 0.2 and 5 Hz. We then differentiate the cubic function to determine the local maximum which we take as the scintillation-rate parameter, ν_c. An example is shown in Figure 21.

The scintillation-rate parameter, ν_c, is affected both by the Fresnel radius and by the relative motion of the irregularities and the radio line of sight. The satellite motion, which is known, usually is the major contributor to the relative motion. In addition, the rate parameter tends to increase under strong-scatter conditions, because of a broadening of the spectrum. In our routine data processing, we measure the spectral summary parameters, T, p, and ν_c, to determine their geometrical dependence and general morphology.

Second-order signal statistics in the spatial and spectral domains are being characterized in terms of correlations between signals received, respectively, on spaced antennas and at various frequencies in the UHF spectrum. As an example, we present results on loss of signal coherence across the band of transmitted UHF spectral lines during a pass over Ancon in December of 1976. In principle, one would like to characterize spectral coherence in terms of the complex mutual coherence function $\langle E(f)E^*(f + \Delta f)\rangle$. Because of the dispersive nature of the ionosphere to radio waves, however, the mutual coherence function can take on a reduced value caused by a deterministic phase trend across a band of frequencies, having little to do with correlation of the statistical fluctuations of interest in characterizing scintillation. Consequently, we have chosen to work directly with the real correla-

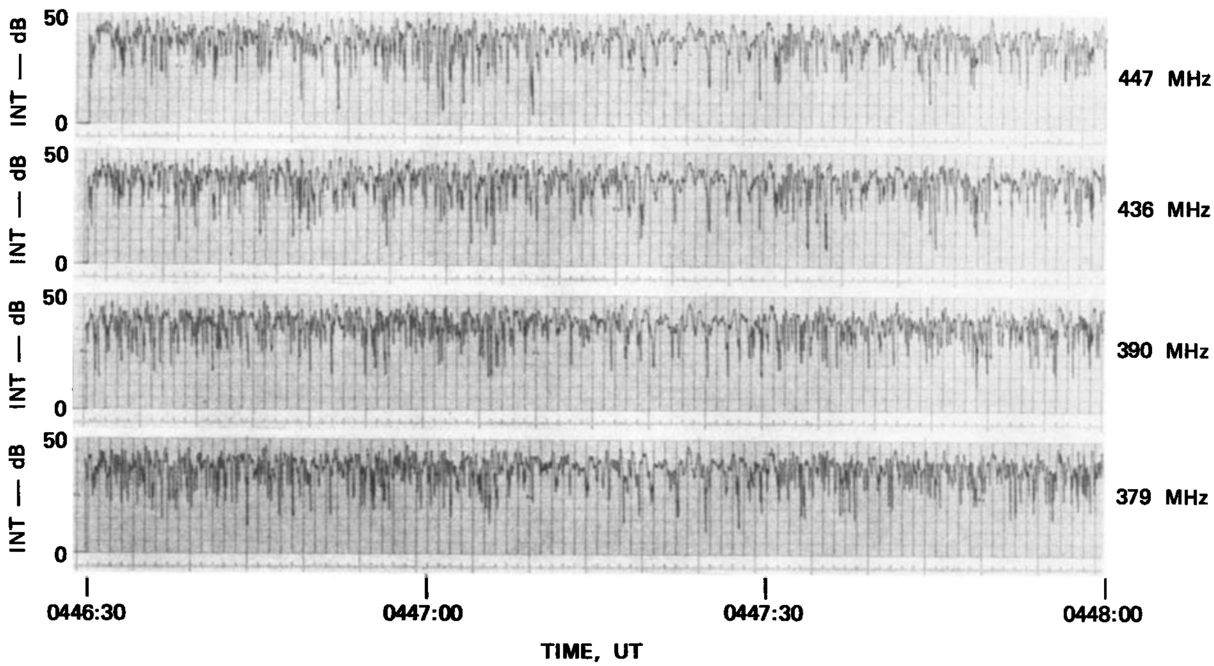

Fig. 23. Portions of four (detrended) UHF intensity records used in correlation analysis presented in Figure 22. Recorded at Ancon on 16 December 1976.

tion functions defined in (6) and (7).

Figure 22 shows the intensity correlation coefficients, defined in (6), for two pairs of UHF spectral lines, as functions of time during the first part of the pass in question. As might be expected, the more widely separated pair (379 and 447 MHz) consistently displays greater decorrelation than does the less widely separated pair (390 and 436 MHz). Also shown on the figure is a graph of $(1 + S_4^2)^{-1/2}$, which is the value that the correlation coefficient defined in (6) would take under conditions of uncorrelated intensity scintillations. Thus, throughout the event there is partial correlation between the intensity fluctuations recorded on the UHF channels analyzed. A portion of the four intensity records used in the correlation analysis is presented in Figure 23 for visual inspection.

Compared with the ordered behavior of the intensity correlation coefficients, the behavior of the phase correlation coefficients for the same frequencies, defined in (7), was more erratic, as illustrated in Figure 24. There is some question about the accuracy of statistical moments of phase calculated under the most severe scintillation conditions. Under such conditions, the routine processing of data decimated to 50 samples per second does not result in a continuous track of all 2π crossings. The data presented in Figures 13 and 24 were processed at the full 500 sample-per-second rate, but it is still possible that some 2π crossings were missed. This may account for some of the less ordered behavior of phase moments as compared with their intensity counterparts. (The basic depar-

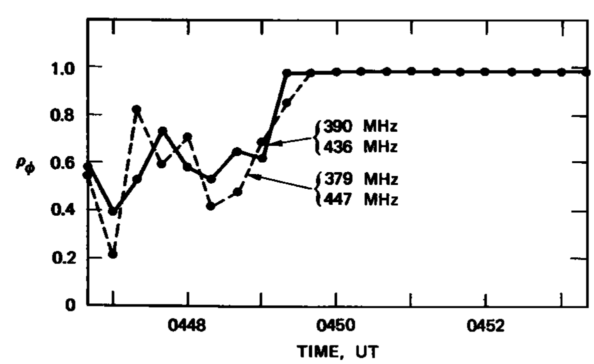

Fig. 24. Spectral decorrelation behavior of UHF phase during portion of pass recorded at Ancon on 16 December 1976. (Data points placed at centers of 20-sec calculation intervals.)

ture of σ_{ϕ} from an f^{-1} behavior illustrated in Figure 13 is thought to be a true diffractive effect, however, since there was virtually no difference in the VHF values calculated at the two data rates.)

Spatial decorrelation analogous to the spectral decorrelation illustrated in Figures 22, 23, and 24 also has been observed. Measurable spatial decorrelation has been observed more frequently, in fact, than spectral decorrelation. Under such conditions, the spaced-receiver records can be employed to glean information about the height and motion of the scintillation-producing irregularities. The results of such analysis, including full cross-spectral processing, will be reported separately.

4. CONTINUING OBSERVATIONS

A large volume of data on transionospheric signal statistics is being collected at the three Wideband experiment receiving stations. Presently, plans are firm only for one year of observations, ending in May 1977. Active consideration is being given, however, to continuing observations at Kwajalein through September and to opening the Ancon and Poker Flat stations in the September-October-November equinoctial period. The routine observing schedule at each of the stations comprises operations during local nighttime hours on Tuesdays, Wednesdays, and Thursdays and during local daytime hours on Wednesdays. This results in about six recordings per week at each of the two low-latitude stations and about twelve per week at the high-latitude station.

The beacon transmits continuously and is expected to continue doing so for several years. It is very likely, in fact, that the transmissions will continue for the better part of the current 11-year solar cycle, although a reduction in duty cycle may be necessary after a few years. The orbit is so nearly circular and its sun-synchronism so stable that several observers do, and many more could, receive the Wideband satellite signals (with relatively broadbeam antennas) without a need for accurate orbital updates. Information to facilitate such observations is available from the authors.

5. CONCLUSIONS

We have presented here a few examples of the results being obtained from observations of the Wideband satellite. Detailed analysis of the data is presently under way. Several conclusions can be drawn from the preliminary observations, however.

First, a large majority of ionospherically imposed scintillation can be adequately modeled in terms of an equivalent phase screen [*Booker et al.*, 1950]. On the other hand, propagation theories based on assumption of weak, single scatter (e.g., the first Born approximation) seldom are appropriate. That is, even moderate intensity scintillation is usually accompanied by phase scintillation (in the same fluctuation-spectral regime) comparable to or greater than a radian. Furthermore, under conditions of even rather well developed intensity scintillation, there usually is little or no decrease in phase variance with increasing Fresnel distance, such as would be predicted, for instance, if one were to apply the Rytov formalism [*Tatarskii*, 1971] to calculation of phase statistics.

All of the foregoing is consistent with production of scintillation in plasma-density irregularities whose spatial spectrum is dominated by large scale sizes. Indeed, the limited spectral analysis carried out thus far on the Wideband signals is consistent with a power-law model for the spatial spectrum. The power-law exponent, however, is not a universal constant for all ionospheric structure. In particular, there appears to be a consistent transition in spectral index associated with enhancement of irregular structure at the subauroral scintillation boundary. This boundary enhancement is a data feature we intend to emphasize in future analysis.

While dominance of the ionospheric spatial spectrum by large-scale structure renders phase-screen modeling useful most of the time, vivid departures from the signal behavior expected in the near zone of a phase screen do occur on occasion. Especially under conditions that produce intensity scintillation at gigahertz frequencies, the signal statistics at lower frequencies are decidedly altered by diffraction effects. The alterations include disruption of the simple f^{-2} frequency dependence of phase variance, and decorrelation of UHF signals as closely spaced as 11.5 MHz.

The preliminary Wideband results, therefore, suggest caution in applying differential-phase measurements performed at lower frequencies to prediction of propagation conditions at gigahertz frequencies, for two reasons. First, under conditions of interest, one would not know if phase scintillations on the reference channel in a VHF/UHF coherent receiver were correlated with phase scintillations in the measurement channel or not. Even accepting this uncertainty in the measurement, one could not safely apply a universal scaling law to apply VHF phase measurements to predictions of L-band phase scintillation. An f^{-2} scaling of phase variance, for instance, would underestimate the L-band variance by an unknown amount. This may be of some relevance, for instance, in planning for L-band imaging systems such as SEASAR (the synthetic aperture radar on SEASAT).

A topic to be emphasized in our future analysis will be the variability of scintillation frequency dependence, including comparison with theoretical calculations. We intend to explore also—probably in many of the same records—conditions under which frequency diversity might conceivably be a viable means of combating scintillation, because of spectral decorrelation. The strong diffraction effects contained in such records occur both at auroral and equatorial latitudes. For the most part, however, the greatest extremes in scintillation—both the most disturbed and the most benign—conditions occur near the geomagnetic equator.

Acknowledgments. The Wideband satellite experiment is being performed for the Defense Nuclear Agency (DNA) under contract DNA001-75-C-0111. The authors acknowledge with appreciation the many contributions made by D. E. Evelyn, of DNA, to the development and fielding of the experiment. The receiving station at Ancon, Peru, is operated by personnel of the Instituto Geofisico del Peru, under the direction of J. Pomalaza. The location of the receiving station at the Poker Flat Rocket Range near Fairbanks was made possible by the Geophysical Institute of the University of Alaska.

REFERENCES

Aarons, J., J. P. Mullen, and H. E. Whitney (1969), The scintillation boundary, *J. Geophys. Res.*, *74*(3), 884-889.

Basu, S., S. Basu, and B. K. Khan (1976), Model of equatorial scintillations from in-situ measurements, *Radio Sci.*, *11*(10), 821-832.

Booker, H. G., J. A. Ratcliffe, and D. H. Shinn (1950), Diffraction from an irregular screen with applications to ionospheric problems, *Phil. Trans. Roy. Soc.*, *A242*, 579-607.

Bowles, K. L. (1963), Measuring plasma density in the magnetosphere, *Science*, *139*, 389-391.

Bramley, E. N. (1955), Some aspects of the rapid directional fluctuations of short radio waves reflected at the ionosphere, *Proc. Inst. Elec. Eng.*, *102*, 533-540.

Briggs, B. H., and I. A. Parkin (1963), On the variation of radio star and satellite scintillations with zenith angle, *J. Atmos. Terr. Phys.* *25*(6), 339-366.

Burns, A. A., and E. J. Fremouw (1970), A real-time correction technique for transionospheric ranging error, *IEEE Trans. Antennas Propagat.*, *AP-18*(6), 785-790.

Dyson, P. L., J. P. McClure, and W. B. Hanson (1974), *In situ* measurements of the spectral characteristics of F region ionospheric irregularities, *J. Geophys. Res.*, *79*(10), 1497-1502.

Klobuchar, J. A., (Ed.) (1973), Total electron content studies of the ionosphere, AFCRL-TR-73-0098, Air Force Survey in Geophysics, *No. 257*, Air Force Cambridge Research Laboratories, L. G. Hanscom Field, Bedford, Mass.

Leadabrand, R., M. J. Baron, J. Petriceks, and H. F. Bates (1972), Chatanika, Alaska, auroral-zone incoherent-scatter facility, *Radio Sci.*, *7*(7), 747-756.

Phelps, A. D. R., and R. C. Sagalyn (1976), Plasma density irregularities in the high-latitude topside ionosphere, *J. Geophys. Res.*, *81*(4), 2059-2064.

Rino, C. L., and E. J. Fremouw (1973), Statistics for ionospherically diffracted VHF/UHF signals, *Radio Sci.*, *8*(3), 223-233.

Rufenach, C. L. (1971), A radio scintillation method of estimating the small-scale structure in the ionosphere, *J. Atmos. Terr. Phys.*, *33*, 1941-1951.

Skinner, N. J., R. F. Kelleher, J. B. Hacking, and C. W. Benson (1971), Scintillation fading of signals in the SFH band, *Nature Phys. Sci.*, *232*, 19-21.

Tatarskii, V. I. (1971), *The Effects of the Turbulent Atmosphere on Wave Propagation*, 472 pp., National Technical Information Service, Springfield, Va.